An *in-vivo* digital atlas of the spatially reliable cerebral vasculature in mice

Rukun Hinz[1], Meriam Malekzadeh[1], Lore M. Peeters[1], Verdi Vanreusel[1], Marleen Verhoye[1],

Annemie Van der Linden[1], Georgios A. Keliris[1]*

[1]Bio-Imaging Lab, University of Antwerp, Belgium

*Corresponding author

Prof. Georgios Keliris

Bio-imaging lab, University of Antwerp

Campus Drie Eiken– Building Uc 1.07

Universiteitsplein 1 -2610 Wilrijk – Belgium

Tel. +32322652772

Email: Georgios.Keliris@uantwerpen.be

Keywords: Digital cerebral vascular atlas, Mouse, Resting-state functional MRI, Vascular skeleton, Magnetic Resonance Imaging, Angiography, TOF MRA

Abstract

Cerebral vascular abnormalities can have a large impact on brain function and have been frequently detected as a comorbidity in various neuropathologies. The mouse is the most common pre-clinical animal model used to investigate neuropathologies and thus cerebral vascular atlases of this species are indispensable. In particular, an atlas derived from multiple animals and that can address inter-subject variability is still absent. The current study presents a mouse cerebral vascular atlas developed from MR 2D-TOF angiograms acquired from a relatively high number (N=21) of 12 weeks old male C57BL/6 mice. The vascular atlas we present depicts large arteries, veins and sinuses that are more spatially reliable across animals than smaller vessels. The atlas is available for download and contains multiple datasets: i) a cerebral vascular atlas; ii) a digital segmentation of large vessels (arteries and veins); iii) a high resolution T2 anatomical background aligned to the atlas; iv) a skeletonized vascular atlas; and v) a vascular graph model. We suggest that these components provide a very potent analysis tool for mouse fMRI data and that the atlas can be used as a template for multimodal brain imaging studies. To this end, we also demonstrate an explicit application of the atlas for the investigation of vascular influences in resting-state fMRI.

1. Introduction

The cerebral vasculature has an indispensable supporting role in maintaining the energy homeostasis of the brain by supplying it with oxygen and nutrients as well as clearing the brain of waste metabolites. [1, 2]. Any structural aberrations in the cerebral vasculature, such as those due to stroke, can deplete the continuous blood supply and can result in cell death and loss of function. Furthermore, structural vascular abnormalities have been shown to commonly arise as comorbidities in various neuropathological disorders, such as Alzheimer's disease, Huntington's disease and multiple sclerosis [3–5]. Hence, appropriate sensitive tools to investigate cerebral vasculature are required.

In preclinical research, mice models are by far the most commonly used animal models to study neuropathological disorders. During the last decades, technological advancements have been made in preclinical imaging allowing for the characterization of the mouse brain's vasculature at different spatial scales. For example, *ex-vivo* imaging techniques like knife-edge scanning microscopy (KESM), micro-optical sectioning tomography (MOST), serial two photon tomography and light sheet microscopic (LSM) imaging have been used to acquire high-resolution imaging data of the vascular architecture up to the capillary level [6–11]. These techniques result in the acquisition of large datasets that allow in-depth analysis of the whole brain vasculature. Furthermore, *in-vivo* imaging techniques, such as computed tomography (CT), magnetic resonance angiography (MRA) and transcranial functional ultrasound (fUS) have been optimized to visualize cerebral vasculature with its main advantage that it can follow-up vascular integrity in the same subject over time [12–14]. These latter techniques predominantly image the macro vasculature, but CT and MR imaging

57   can also be performed *ex-vivo* with longer acquisitions and higher resolution to acquire

58   information about the microvasculature [15, 16]. Using the aforementioned techniques,

59   several vascular atlases have been developed to assist in identifying the mouse brain

60   vasculature. In one study, *ex-vivo* CT imaging was combined with MRI to image the mouse

61   whole brain vasculature of four mice together with an anatomical background [17]. This atlas

62   provides the segmentation of the vasculature at the macroscopic level allowing the

63   identification of most large vessels. A more detailed vascular atlas was obtained in the study

64   of Xiong et al. using micro-optical sectioning tomography (MOST) [18]. In that study, the

65   entire mouse brain vascular architecture was mapped of five animals and up to the capillary

66   level allowing the identification of the whole brain vasculature as well as the investigation

67   of microvascular densities in the brain.

68   Knowledge of the vascular architecture is not only important for identifying vascular

69   alterations in disease states but can also play a key role in supporting a variety of

70   neuroimaging techniques. Imaging studies such as fUS and intrinsic optical imaging (IOS)

71   are exclusively based on acquiring vascular information, but with limited spatial resolution

72   [19, 20]. Vascular atlases that would be suitable to use across studies and incorporate

73   anatomical information can help to identify the spatial location of the vessel. Furthermore,

74   vessel occlusion studies that investigate stroke can benefit from vascular atlases to select the

75   appropriate vessel to occlude or to estimate the size of the hypoxic area. An important number

76   of studies that can benefit from vascular atlases are those using functional MRI (fMRI) and/or

77   resting state fMRI (rsfMRI). These techniques rely on the acquisition of blood oxygenation

78   level dependent (BOLD) signals that are mainly derived from the hemodynamic responses

79   caused by the neurovascular coupling [21]. However, studies have shown that other vascular

80   effects, such as vascular drainage, also influence the BOLD signal [22, 23]. Additionally,

81   resting state signals have been shown to be confounded by signals from large arteries and

82   veins [24]. These confounding signals are thought to be systemically produced from outside

83   the brain and seem to be propagating throughout the blood vessels [25]. A vascular atlas that

84   can be readily used in such studies, can help in identifying potential vascular confounds and

85   assist in further analysis steps aiming to remove them.

86   To be able to apply a vascular atlas in the aforementioned studies, it is assumed that the

87   spatial location of the vasculature is conserved between subjects. However, the study of

88   Xiong et al. has shown that the spatial location of small vessels (< 40 μm) can be highly

89   variable between subjects of the same strain, while larger vessels (> 40 μm) are more spatially

90   reliable [18]. An efficient method to visualize spatially reliable vessels is to develop a

91   vascular atlas based on angiograms from multiple subjects. As such, spatial unreliable vessels

92   will be suppressed by averaging the datasets. However, mouse vascular atlases to date

93   focused on the visualization of the detailed vasculature in a single mouse or a small number

94   of subjects and were created *ex-vivo* in order to use techniques that allow high resolution [18,

95   26]. Thus, existing mouse vascular atlases are less suitable for application across studies.

96   In this study, we developed and present an *in-vivo* acquired cerebral vascular atlas of the

97   large vessels using 21 male C57BL/6 mice of 12 weeks of age. To this end, non-invasive

98   imaging, 2D time of flight (TOF) MRA was used and combined with high-resolution

99   anatomical T2-weighted MRI for spatial identification. Our digital atlas is provided together

100   with an anatomical MRI template, and thus allows easy and direct co-registration to MRI

101   datasets or can be used as a reference template for segmenting newly acquired individual

102   angiography. We also provide a skeletonized version of the atlas that can be used as a graph

103   to calculate parameters such as path length. Moreover, in this study, we demonstrate an

104   explicit application of the atlas for the investigation of vascular influences in resting-state

105   fMRI by estimating the overlap between vasculature and resting state networks (RSNs).

106   **2.   Material and Methods**

107   **2.1. Animals and ethical statement**

108   The study was conducted using 12 weeks old male C57BL/6 wild-type mice (N=21)

109   (Janvier). Mice were kept under a day/night cycle of 12h/12h respectively, with an average

110   room temperature of 20-24°C and 40% humidity. All mice were group housed with *ad libitum*

111   access to water and standard rodent chow. All applicable institutional and/or national

112   guidelines for the care and use of animals were followed. Procedures were performed in

113   accordance with the European Directive 2010/63/EU on the protection of animals used for

114   scientific purposes. The protocols were approved by the Committee on Animal Care and Use

115   at the University of Antwerp, Belgium (permit number: 2016-10) and all efforts were made

116   to minimize animal suffering. Experiments have been reported in compliance with the

117   ARRIVE guidelines.

118   **2.2. Data availability statement**

119   Data   used   in   this   study   are   available   online   and   can   be   downloaded   at

120   www.uantwerpen.be/en/research-groups/bio-imaging-lab/research/mri-atlases/.   Datasets

121   include 2D-TOF MRA of each individual subject, vascular atlas, skeletonized version of the

122   vascular atlas and the anatomical study-specific template.

123   **2.3. Imaging procedure**

124   All MR imaging procedures were performed on a 9.4 T Biospec MR system (Bruker,

125   Germany) with a receive-only 4 channel array cryoprobe (Bruker, Germany) combined with

126   a volume transmit resonator. All animals underwent MRA imaging, whereas a partial group

127   (N=13) was scanned a second time to extract rsfMRI data.

128   **2.3.1.   MRA imaging**

129   For MRA imaging, animals were first anesthetized using 5% isoflurane in a gas mixture of

130   30% O2 and 70% N2 for induction, which was then subsequently decreased to 2% isoflurane

131   for maintenance during the remainder of the session. All mice were placed head-fixed in the

132   scanner by using ear- and tooth-bars and ophthalmic ointment was applied to the eyes to

133   prevent desiccation. During the experimental procedure, animals' physiology was closely

134   monitored. As such, respiratory rate was followed using a pressure sensitive pad (MR-

135   compatible Small Animal Monitoring and Gating system, SA Instruments, Inc.). Body

136   temperature was followed using a rectal thermistor and was maintained at (37.0 ± 0.1) °C

137   using a feedback controlled warm air heat system (MR-compatible Small Animal Heating

138   System, SA Instruments, Inc.). Additionally, blood oxygenation was monitored using a pulse

139   oxygenation meter (MR-compatible Small Animal Monitoring and Gating system, SA

140   Instruments, Inc.).

141   MRI data acquisition consisted out of the measurement of three orthogonal oriented 2D-TOF-

142   MRA to assess the macrovasculature with blood flow in each direction: (FOV: (20x20) mm²,

143   matrix dimension (MD: [320x320], 110, 130, 90 slices respectively in the coronal, axial and

144   sagittal oriented scans, slice thickness (ST): 0,3 mm, slice shift: 0.15 mm, voxel dimension

145    $(0.0625x0.0625x0.15)$ mm³, TE/TR: 3.2/17 ms, flip angle: 60°,number of averages: 3).

146   Subsequently, a high-resolution 3D T2-weighted Turbo-RARE was acquired for the

147   development of an anatomical template (FOV: (20x20x15) mm², MD: [256x256x192], voxel

148   dimension = $(0.078$ mm)³, TE/TR: 40/2500 ms, RAREfactor: 16). After the imaging

149   procedure, animals were kept in a recovery box with infrared heating until they were fully

150   awake to compensate for post-anaesthethic decreased body temperature.

151   2.3.2.   Resting state functional MRI

152   RsfMRI was acquired 1 to 2 weeks after the MRA imaging session. To do so, animals'

153   anesthesia was first induced with 5% isoflurane in a gas mixture of 30% O_2 and 70% N_2 and

154   was lowered to 2% isoflurane for maintenance. Mice were head-fixed and were monitored

155   similarly as for the previous MRA session. Ophthalmic ointment was applied to the eyes.

156   After fixation, animals received a subcutaneous bolus of medetomidine (0.05 mg/kg) which

157   was 15 minutes later followed by a subcutaneous continuous infusion of medetomidine (0.1

158   mg/kg/h). After bolus injection, isoflurane concentration was gradually decreased to 0.4%

159   isoflurane over a time period of 5 minutes.

160   In each animal, three orthogonally placed T2-weighted Turbo-RARE (FOV: (20x20) mm²,

161   MD: [256x256], 12 slices, ST: 0.4 mm, TE/TR: 33/2500 ms, RAREfactor: 8) anatomical

162   images were acquired to ensure slice position uniformity between animals. Next, a coronal

163 oriented T2-weighted anatomical reference scan was acquired using a Turbo-RARE

164 sequence (FOV: (24x16) mm², MD: [256x256], 16 slices , ST: 0.5 mm, TE/TR: 33/2500 ms,

165 RAREfactor: 8) to be used as an anatomical background for functional imaging data.

166 Afterwards, B0 field maps were acquired to estimate magnetic field inhomogeneity that was

167 used for the subsequent local shimming procedure within a rectangular volume of interest

168 covering the mouse brain. Thirty minutes post-bolus injection, rsfMRI scans were acquired

169 using a T2*-weighted single shot echo planar imaging (EPI) sequence (FOV: (24x16) mm²,

170 MD: [96x64], 16 slices , ST: 0.5 mm, voxel dimension: (0.25 x 0.25 x 0.50) mm³, TE/TR:

171 16/1000 ms, 600 volumes). After the imaging procedure, mice received a subcutaneous bolus

172 injection of 0.1 mg/kg atipamezole (Antisedan, Pfizer, Karlsruhe, Germany) to counteract

173 the effects of medetomidine and then the animals were placed in a recovery box with infrared

174 heating until they were fully awake.

175 **2.4. Data Processing**

176 **2.4.1.   Anatomical Template**

177 The 3D-T2 weighted anatomical scans of each subject were used to develop a study-specific

178 anatomical template. All co-registration processing was performed using Advanced

179 Normalization Tools (ANTS). Scans were first debiased to equalize signal intensities over

180 the FOV. Afterwards, the template was created using the standard ANTS create template

181 protocol.

182 **2.4.2.   MRA**

183   The 2D-TOF MRA sequence is an excellent tool for non-invasive imaging of the complete

184   mouse brain vasculature. This sequence allows for the detection of vascular flow

185   perpendicular towards the slice direction. Therefore, three orthogonally oriented 2D-TOF

186   MRAs were used to visualize vascular flow in the rostral-caudal (fig.1A), dorsal-ventral

187   (fig.1B) and left-right (fig.1C) direction. To develop subject specific angiograms, scans were

188   first visually inspected for motion artifacts and then combined using a maximum Intensity

189   Projection (MIP) (fig.1D). Afterwards, each subject vascular angiogram was co-registered to

190   the anatomical template by using the previously estimated subject to template transformation

191   parameters from the template creation step. Finally, co-registered vascular angiograms of

192   each subject were averaged across all subjects to create a vascular atlas.

193   Next, processing of the data was performed in Amira 5.4 (FEI, Thermo Scientific). Individual

194   blood vessels were manually delineated on the vascular atlas and labeling was based on

195   previous reported vascular atlases [17, 18]. Afterwards, the vascular atlas was skeletonized

196   using Amira 5.4 skeletonization tool transforming the developed atlas into a nodes and edges

197   model. This model was then saved as centerline voxels in Amira 5.4 which converts the nodes

198   and edges model into single voxel lines representing the inner core of the vessels.

199   Additionally, the nodes and edges model allowed for automatic clustering of enclosed

200   circuits. As the circuits of large arteries and veins did not overlap, the nodes and edges model

201   facilitated the automatic separation of arteries and veins. Information coming from the nodes

202   and edges model was then used to develop a vascular graph model in Matlab code (MATLAB

203   R2019a, The MathWorks Inc. Natick, MA, USA).

204

2.4.3. Resting state functional MRI

Data processing was performed using SPM 12 (Statistical Parametric Mapping, http://www.fil.ion.ucl.ac.uk), Gift toolbox (Group ICA of fMRI toolbox version 3.0a: http://icatb.sourceforge.net) and Matlab 2014a (MATLAB R2014a, The MathWorks Inc. Natick, MA, USA). Functional data was first realigned using a 6-parameter (rigid body) spatial transformation. Next, images were used to create a study-specific EPI template by normalizing the first volume EPI of each subject to the first volume of a single subject by using a global 12-parameter affine transformation followed by a non-linear transformation and an averaging of all normalized scans. Afterwards, individual subject functional datasets were normalized to this study-specific EPI template using a global 12-parameter affine transformation and subsequently a non-linear transformation. Normalized data was then smoothed in-plane by using a Gaussian kernel with a full-width half-maximum of twice the voxel size (0.5 x 0.5 mm). Data were then further band pass filtered between 0.01-0.15 Hz.

To extract RSN from rsfMRI data, an independent component analysis (ICA) was performed with the Infomax algorithm with 15 pre-defined number of components. Components representing RSN were calculated by performing a one-sample t-test to obtain distinct networks and identified by comparison to previously observed RSNs [27–30]. ICA data was then co-registered from the EPI template space to the vascular atlas high-resolution 3D-T2 weighted anatomical template space by performing a rigid, affine and non-linear transformation using the ANTS toolbox. For this transformation, each voxel index from the lower resolution EPI data was used as a value instead of a binary mask so that we could calculate overlap with the original EPI voxels after nearest neighbor interpolation. To identify

227 RSNs with potential vascular influences, RSNs were sorted based on the percentage overlap

228 with the vascular atlas. To this end, for each RSN, the vascular overlap fraction (VOF) was

229 calculated by dividing the total amount of (unique) voxels overlapping with the vascular

230 skeleton by the total amount of unique voxels of that RSN.

231
$$VOF = \frac{\# \; voxels \; vascular \; skeleton \; within \; RSN}{\# \; voxels \; RSN}$$

232 Similarly, we calculated partial VOF for specific vascular compartments (i.e. arterial,

233 venous/sinous) or specific vessels by replacing the total vascular skeleton with the skeleton

234 of the vascular compartment of interest

235
$$pVOF = \frac{\# \; voxels \; specific \; vascular \; skeleton \; within \; RSN}{\# \; voxels \; RSN}$$

236 After sorting, the two RSNs with the highest vascular overlap were selected and further

237 analyzed in order to identify the specific arteries and vessels overlapping with these RSNs.

238 To this end, the percentage of vessel inclusion (PVI) within each network was calculated for

239 each artery and vein by dividing the number of voxels of each RSN overlapping with each

240 vessel's skeleton with the number of voxels of that vessel's skeleton and converting to

241 percentage.

242
$$PVI = \frac{\# \; voxel \; RSN \; within \; vessel \; skeleton}{\# \; voxels \; vessel \; skeleton} * 100$$

243

244

3. Results

3.1. Vascular atlas

The 2D-TOF MRA data of 21 male C57BL/6 wild-type mice was used for the development of the vascular atlas. The segmentation resulted in delineation of the main large vessels that were spatially reliable across the sample of 21 mice. Furthermore, the segmentation was sorted into arteries (fig.2) and veins/sinuses (fig.3) to have a clear description of the vascular architecture (further described below). Given the limited spatial resolution of *in-vivo* MRA as well as the inter-subject small variability in vessel positions, the vessel sizes were substantially overestimated. To overcome this limitation, centerlines of the blood vessels were extracted by performing a skeletonization on the segmented data (fig.4). These centerlines depict the vascular atlas in single voxel lines representing the inner core of the blood vessels, which is also the position of highest inter-subject spatial reliability. Given this property, such an atlas representation is especially useful for investigating vascular effects of specific vessels in imaging data. Moreover, the skeletonization also allowed the development of a vascular graph, which represents the hierarchical structure of the vasculature and allows more explicit types of analyses, such as intervascular distance between vessels (or vessels and voxels), branching order, parent-child relationships, *et cetera*.

3.1.1. Arteries

The major arterial system of the mouse brain is visually depicted in figure 2A and its hierarchical graph (fig. 2B) gives an overview of its connections. The blood supply to the mouse brain is provided via four main arteries *i.e.* (i) the two **vertebral arteries** that mainly supply blood to the arteries of the brain stem and the cerebellum and (ii) the two **internal**

267   **carotid arteries** that mainly supply blood to arteries feeding the subcortical and cortical brain

268   regions.

269   The **vertebral artery** depicted one clear branch giving rise to the **para-olivary artery**

270   providing blood towards the inferior olive region. The two vertebral arteries then merge in

271   the midline into the **basilar artery** that is located on the ventral surface of the brainstem until

272   it reaches the pons/midbrain junction to give rise to two **superior cerebral arteries**. These

273   superior cerebral arteries end up in the **lateral and medial superior cerebellar artery**.

274   The **internal carotid artery** branches in rostral, lateral and caudal direction resulting in the

275   **anterior, middle and posterior cerebral artery** respectively. The **anterior cerebral artery**

276   of both internal carotid arteries heads rostrally on the ventral part of the brain and merges

277   together medially to form the **azygos of the anterior cerebral artery**. This artery is directed

278   dorsally and provides blood to the frontal lobe of the brain, including the olfactory bulb and

279   orbitofrontal regions by branching into the **lateral orbitofrontal artery** and later the **medial**

280   **orbitofrontal artery**. Next, the **azygos of the anterior cerebral artery** curves rostral and

281   gives rise to the **azygos pericallosal artery** that runs over the dorsal part of the corpus

282   callosum delivering blood to posterior-medial parts of the frontal-, parietal and temporal

283   lobes. The **middle cerebral artery** branches off from the lateral side of the internal carotid

284   artery and extends over the surface of the ventral part of the brain where it feeds blood to the

285   hypothalamus, caudate putamen and amygdala. It then continues in the dorsal direction on

286   the surface of the brain to provide blood to most of the cerebral cortex. The **posterior**

287   **cerebral artery** is dorsally directed where it is providing blood towards the caudal part of

288   the cerebrum including the hippocampus and the superior colliculus as well as cortical areas.

289   Furthermore, the posterior cerebral artery connects with the superior cerebral artery via the

290   **posterior communicating artery**.

291   At the ventral part of the brain around the level of the optic chiasm and the hypothalamus,

292   the arterial system forms a circulatory anastomosis called the **circle of Willis** (COW). This

293   anastomosis connects the internal carotid artery and the vertebral artery. The circle of Willis

294   is built from the **basilar artery,** which connects to both **superior cerebral arteries** that are

295   both connected with the **posterior cerebral arteries** via the **posterior communicating**

296   **artery**. The two **posterior cerebral arteries** are each connected with an **internal carotid**

297   **artery** that gives rise to the **medial cerebral artery** and the **anterior cerebral artery**. The

298   anterior cerebral artery of both sides fuse into a circular anastomosis.

299   ### 3.1.2.   Veins and Sinuses

300   The major mouse-brain venous system produces a drainage system to remove blood

301   containing low nutrients as well as waste metabolites from the brain. The 2D-TOF MRA

302   detected the dorsal venous system as well as the deep venous system. Furthermore, veins

303   outside of the brain were observed and labeled. The venous system of the mouse brain is

304   visualized in figure 3A and its venous graph (fig. 3B) gives an overview of the connections

305   of each vein.

306   The detected dorsal venous system contains mainly four sinuses and their connecting veins.

307   The most rostral detected sinus is the (i) **superior olfactory sinus** which is connected in the

308   caudal direction with the (ii) **superior sagittal sinus**. These sinuses are located dorsally on

309   the pial surface and cover the midline of the cerebral cortex brain. In the rostral end, the

310   superior sagittal sinus produces the **rostral rhinal veins** in the ventral direction that reaches

311 the frontal lobe. At the caudal end, the superior sagittal sinus splits into two lateral-ventral

312 oriented (iii) **transverse sinuses** that are each connected with a caudal medial oriented (iv)

313 **sigmoid sinus**. The aforementioned sinuses cover most of the pial surface of the cerebral

314 cortex. The transverse sinus was observed to have three branches *i.e.* a ventral directed

315 **medial collicular vein** that penetrates into the cerebral tissue to reach the colliculus areas,

316 the **parafloccular vein** that is directed caudally and reaches the paraflocculus, and finally

317 the rostral directed **caudal rhinal vein**.

318 The deep venous system branches off from the medial-dorsal part of the transverse sinus and

319 gives rise to the **straight sinus**. The sinus is rostroventrally directed and gives rise to the

320 **inferior sagittal sinus** as well as the **vein of Galen**. The vein of Galen was then observed to

321 produce two lateral oriented **longitudinal hippocampal veins** and further caudally two

322 **thalamostriatal veins**.

323 The venous blood is removed from the brain via venous outflow systems. Here the 2D-TOF

324 MRA detected the dorsal and caudal outflow. The dorsal outflow starts from the **nasal**

325 **emissary vein**, which is connected with the rostral part of the superior sagittal sinus. This

326 vein is oriented laterally and merges together with the **supraorbital vein** coming from the

327 eyes into the **superior temporal vein**. The caudal outflow system occurs from the

328 **retroglenoid vein** that is connected to the transverse sinus. The retroglenoid vein and the

329 superior temporal vein merges into the **posterior facial vein** that will eventually remove the

330 venous blood from the head via the external jugular vein.

331 **3.1.3. Skeletonization**

332   The developed 2D-TOF MRA atlas overestimates the vessel size. This is especially clear

333   when comparing the anatomical background images, where vessels produce hypo-intense

334   signals, with the 2D-TOF MRA data (fig. 4B). To overcome this, the vascular atlas was

335   further processed to only visualize the centerlines of each vessel using a skeletonization

336   process. By doing so, the whole brain vasculature could be represented by nodes and edges

337   model or with center lines with a width of one voxel (fig.4). Furthermore, this skeletonization

338   process allows for the development of a vascular graph model (see fig. 2B, 3B), visualizing

339   the hierarchical structure of the vascular architecture.

340   **3.2. Resting state functional connectivity**

341   Functional MRI sequences that rely upon the detection of the BOLD contrast such as gradient

342   echo EPI, are known to suffer from vascular influences especially due to large vessels. In this

343   study, rsfMRI data from a subset of animals used to build the reported atlas, were used to

344   investigate the extent of overlap between RSNs and the major mouse brain vasculature. The

345   RSNs were extracted from functional MRI data using independent component analysis (ICA)

346   and revealed nine functionally relevant networks (suppl. fig. 1). To calculate the percentage

347   overlap between the vasculature and the identified RSN components, we used the

348   skeletonized version of our atlas. Given that the skeletonized atlas has a single voxel

349   resolution, the overlap essentially finds voxels of the resting state network in which major

350   blood vessels are present. The results indicated that a number of networks demonstrated

351   substantial fraction of major vascular overlap (suppl. table 1). Specifically, the VOF values

352   were as follows sorted from highest to lowest overlap: Cingulate-Retrosplenial I = 0.06,

353   Cingulate – Retrosplenial II = 0.0483, Orbitofrontal = 0.0428, Hippocampal = 0.0417,

354   Striatum = 0.024, Somatosensory barrel field = 0.0239, Somatosensory – Motor = 0.0184,

355   Primary somatosensory = 0.0183, Visual Cortex = 0.0167. The two networks with the highest

356   VOF were both networks which include the cingulate and retrosplenial cortex *i.e.* cingulate-

357   retrosplenial (Cg-Rs) I and II (fig. 5). Specifically, Cg-Rs I and Cg-Rs II components

358   demonstrated values of around 6% and 5% of voxels with overlap with major mouse

359   vasculature respectively. The Cg-Rs I network was observed to include the complete

360   cingulate cortex and partially the retrosplenial cortex as well as motor cortex, preoptic area,

361   dorsal thalamus, superior colliculus and hippocampus. The Cg-Rs II network contained only

362   the posterior part of the cingulate, the entire retrosplenial cortex as well as the parietal

363   association and visual cortex. The substantial overlap of these networks with the major mouse

364   vasculature can directly be appreciated on the 3D visual representation of these components

365   as shown in figure 6 (fig. 6). Another two networks demonstrated substantial vascular overlap

366   of over 4% of voxels was the orbitofrontal and hippocampal networks, while all other

367   networks demonstrated vascular overlap values < 2.5%.

368   To better understand the contribution of the arterial and venous/sinous compartments as well

369   as the contribution of specific vessels within each of the two cingulate – retrosplenial

370   networks, we also calculated the partial VOF (pVOF) for each vessel (table 1).

371   The Cg-Rs I network includes arteries, veins and sinuses while Cg-Rs II contained mainly

372   veins and sinuses. In the Cg-Rs I, a venous overlap could be seen from the superior sagittal,

373   transverse and the straight sinuses including all its labeled branches. The arterial overlap of

374   the Cg-Rs I involved the internal carotid artery, anterior cerebral artery and its branches, the

375   posterior/middle cerebral artery and the superior cerebellar artery. The Cg-Rs II vascular

376   overlap contained mainly venules *i.e.* the superior sagittal sinus and the straight sinus and its

377   branches. Arterial overlap was limited to the superior/middle cerebral artery, azygos

378   pericallosal artery and the medial orbitofrontal artery.

379   **4. Discussion**

380   An intact vascular architecture is essential for the healthy function of the brain. It is therefore

381   of utmost importance for many studies to be able to evaluate the contribution of vessel signals

382   and/or detect vascular abnormalities. Previously developed mouse cerebral vascular atlases

383   mainly focused on the visualization of the - as much as possible - complete vascular tree

384   down to the small vessels and capillaries. This resulted in high-resolution large datasets that

385   tend to be time consuming to acquire and difficult to process [31] and therefore report results

386   from a limited number of animals [17, 18]. In the current study, we developed of a mouse

387   cerebral vascular atlas that focusses on visualizing the spatially reliable larger vessels in a

388   high number of C57BL/6 wild-type mice (N=21) at the age of 12 weeks. In contrast to

389   previous atlases, this atlas was specifically developed to be used as a reference vascular atlas

390   for group analysis across studies that use C57BL/6 wild-type mice. By using high number of

391   animals, the averaging of the individual cerebral vasculature enhances spatial reliable vessels

392   and suppresses vessels demonstrate anatomical variations across subjects. In addition, the

393   vascular atlas is co-registered to high-resolution anatomical data which is adding spatial

394   information to the vasculature.

395   **4.1. 2D-TOF MRA**

396   The vascular atlas was developed using a 2D-TOF MRA sequence. This MRI sequence was

397   specifically chosen for its high sensitivity towards the vasculature and its complete non-

398   invasiveness, which allows for easy implementation in future MRI studies. The method

399   allowed for the detection of blood vessels based upon their flow perpendicular to the slice

400   position. It was therefore required to acquire three orthogonally positioned 2D-TOF MRA

401   scans to obtain the complete overview of the vasculature. The 2D-TOF MRA was chosen

402   instead of its 3D-TOF MRA counterpart due to its superior sensitivity to slow flow allowing

403   for the detection of a wider range of vessels. Moreover, 3D-TOF MRA is also more sensitive

404   to motion artifacts that could compromise the data acquisition. By combining three 2D-TOF

405   MRA datasets, we implemented a method for non-invasive reproducible detection of *in-vivo*

406   cerebral vasculature in mice.

4.2. Vascular atlas

407

408   The presented *in-vivo* vascular atlas contains multiple datasets: i) a cerebral vascular atlas;

409   ii) a digital segmentation of large vessels (arteries and veins/sinuses); iii) a high resolution

410   T2 anatomical background; iv) a skeletonized vascular atlas; and v) a vascular graph model.

411   The cerebral vascular atlas is an average vascular template created by all co-registered 2D-

412   TOF MRA datasets and is accompanied by a T2-weighted anatomical template. These

413   datasets can be used as a co-registration endpoint to acquire either vascular information or

414   anatomical information. The templates will be especially useful for studies that acquire 3D

415   anatomical information (MRI, CT) and want to extract cerebral vascular information or for

416   studies that rely on the acquisition of vascular information (fUS, IOS) and want to get

417   anatomical information. The vascular atlas was manually segmented, which resulted in the

418 labeling of spatially reliable vessels. The segmentation included the main large arteries, veins

419 and sinuses within the brain as well as their outflow systems going around the head. However,

420 small branches were not included due to spatial variation between subjects. The anatomical

421 structure of the vessels was similar as in the paper of Xiong et al. that produced a high

422 resolution *ex-vivo* vascular atlas in the same C57BL/6 mouse strain [18]. Small differences

423 were found between our labeling and the vascular atlas of Dorr et al. that mainly revolved

424 around the posterior communicating artery being connected with the posterior cerebral and

425 internal carotid artery, while in our dataset it was connecting the posterior and superior

426 cerebral artery [17]. However, this can be explained as the aforementioned atlas was acquired

427 in a different mouse strain *i.e.* CBA mouse strain. Previous studies have reported structural

428 cerebral vascular differences between mouse strains [32, 34, 35]. This indicates caution when

429 using the vascular atlas in other strains than the C57BL/6 strain. Furthermore, due to the

430 spatial variability of the cerebral vasculature, the segmentation of the blood vessels were

431 overestimated. To overcome this, the segmentation was skeletonized and vascular centerlines

432 were extracted. As the vascular centerlines depicts blood vessels as single voxel lines it is a

433 more appropriate tool to investigate the spatial location of the vasculature. The centerlines

434 will therefore be of use in studies that are particularly interested in defining the presence of

435 vasculature in their datasets. In addition to the centerlines, the skeletonization process results

436 in a representation of the vasculature as nodes and edges allowing for the development of a

437 vascular graph model. The vascular graph model contains the hierarchical structure of the

438 cerebral vascular architecture and allowed automatic clustering of the arterial and venous

439 system. This model can be used to get insights in blood flow patterns which could be valuable

440 for studies performing BOLD and perfusion analysis.

4.3. Application of the vascular atlas in rsfMRI

RsfMRI relies upon the detection of fluctuations in the BOLD signal, which is assumed to be an indirect measurement of changes in neural activity detected via the neurovascular coupling. As BOLD signals are based on detecting changes in blood oxygenation, it is assumed that it is most sensitive to the capillaries where most of the oxygenation exchange occurs. However, the BOLD signal has been shown to be influenced by the macrovasculature [22]. More specifically, confounding BOLD signals of vascular origin have been widely detected coming from downstream draining veins [22]. This is caused due to the accumulation of the blood coming from the capillaries to the draining veins and thus smearing out the BOLD signal via the venules. Therefore, as an application of the vasculature atlas, we implemented the atlas to rsfMRI data to investigate the vascular contribution in the observed RSN. The vascular overlap analysis could show that the two highest overlapping components were components covering connections between the cingulate and retrosplenial cortex (Cg-Rs I and II). These regions are commonly part of the default mode-like network in mice [27, 29, 36]. Using the vascular atlas, we could reveal that the Cg-Rs I & II RSNs have the strongest vascular contribution, but this is still limited to around 6% and 5% of the original resolution EPI voxels being penetrated by the large, reliable vessels included in our atlas. This indicates that even if these networks suffer from slightly higher vascular influences in comparison to some other networks, the majority of their voxels are not penetrated by the large vessels and thus their functional correlations most probably reflect neuronal components.

5. Conclusion

In conclusion, this article presents a newly developed *in-vivo* mouse brain vascular atlas based on 21 adult male C57BL/6 wild-type mice (12 weeks old) acquired with MRI. The atlas includes: i) a cerebral vascular atlas; ii) segmentation of large vessels; iii) a high resolution T2 anatomical background; iv) a skeletonized vascular atlas; and v) a vascular graph model that are available online for download. The atlas acts as a co-registration template for studies that require both vascular and anatomical information. As a potential application, we superimposed the atlas on rsfMRI data of adult male C57BL/6 wild-type mice which enabled us to identify a differential degree of overlap between the vasculature and the different RSNs. Undoubtedly the use of this atlas will contribute to a more solid interpretation and post processing of resting state data obtained in mice.

6. Acknowledgments

Author contribution statement

Rukun Hinz: Study initiation, Data acquisition, Data processing, Writing of the article

Meriam Malekzadeh: Data processing: vascular segmentation

Lore M. Peeters: Study initiation, Data processing, Writing of the article

Verdi Vanreusel: Data processing: Co-registration

Marleen Verhoye: Study initiation, Writing of the article

Annemie Van der Linden: Study initiation, Writing of the article

Georgios A. Keliris: Study initiation, Data Processing, Writing of the article, Study supervision

Disclosure/conflict of interest

The Author(s) declare(s) that there is no conflict of interest

References

[1] Mergenthaler P, Lindauer U, Dienel GA, et al. Sugar for the brain: the role of glucose in physiological and pathological brain function. *Trends Neurosci* 2013; 36: 587–97.

[2] Jain V, Langham MC, Wehrli FW. MRI estimation of global brain oxygen consumption rate. *J Cereb Blood Flow Metab* 2010; 30: 1598–607.

[3] Govindpani K, McNamara LG, Smith NR, et al. Vascular Dysfunction in Alzheimer's Disease: A Prelude to the Pathological Process or a Consequence of It? *J Clin Med*; 8. Epub ahead of print 10 May 2019. DOI: 10.3390/jcm8050651.

[4] Lin C-Y, Hsu Y-H, Lin M-H, et al. Neurovascular abnormalities in humans and mice with Huntington's disease. *Exp Neurol* 2013; 250: 20–30.

[5] D'haeseleer M, Cambron M, Vanopdenbosch L, et al. Vascular aspects of multiple sclerosis. *Lancet Neurol* 2011; 10: 657–66.

[6] Amato SP, Pan F, Schwartz J, et al. Whole Brain Imaging with Serial Two-Photon Tomography. *Front Neuroanat* 2016; 10: 31.

[7] Mayerich D, Kwon J, Sung C, et al. Fast macro-scale transmission imaging of microvascular networks using KESM. *Biomed Opt Express* 2011; 2: 2888–96.

[8] Xue S, Gong H, Jiang T, et al. Indian-ink perfusion based method for reconstructing continuous vascular networks in whole mouse brain. *PLoS One* 2014; 9: e88067.

[9] Wu J, He Y, Yang Z, et al. 3D BrainCV: simultaneous visualization and analysis of

516   cells and capillaries in a whole mouse brain with one-micron voxel resolution.

517   *Neuroimage* 2014; 87: 199–208.

518 [10] Lugo-Hernandez E, Squire A, Hagemann N, et al. 3D visualization and

519   quantification of microvessels in the whole ischemic mouse brain using solvent-

520   based clearing and light sheet microscopy. *J Cereb Blood Flow Metab* 2017; 37:

521   3355–3367.

522 [11] Todorov MI, Paetzold JC, Schoppe O, et al. Machine learning analysis of whole

523   mouse brain vasculature. *Nat Methods* 2020; 17: 442–449.

524 [12] Starosolski Z, Villamizar CA, Rendon D, et al. Ultra High-Resolution In vivo

525   Computed Tomography Imaging of Mouse Cerebrovasculature Using a Long

526   Circulating Blood Pool Contrast Agent. *Sci Rep* 2015; 5: 10178.

527 [13] Klohs J, Baltes C, Princz-Kranz F, et al. Contrast-Enhanced Magnetic Resonance

528   Microangiography Reveals Remodeling of the Cerebral Microvasculature in

529   Transgenic ArcA Mice. *J Neurosci* 2012; 32: 1705–1713.

530 [14] Tiran E, Ferrier J, Deffieux T, et al. Transcranial Functional Ultrasound Imaging in

531   Freely Moving Awake Mice and Anesthetized Young Rats without Contrast Agent.

532   *Ultrasound Med Biol* 2017; 43: 1679–1689.

533 [15] Quintana DD, Lewis SE, Anantula Y, et al. The cerebral angiome: High resolution

534   MicroCT imaging of the whole brain cerebrovasculature in female and male mice.

535   *Neuroimage* 2019; 202: 116109.

536 [16] Pathak AP, Kim E, Zhang J, et al. Three-dimensional imaging of the mouse

537   neurovasculature with magnetic resonance microscopy. *PLoS One* 2011; 6: e22643.

538 [17] Dorr A, Sled JG, Kabani N. Three-dimensional cerebral vasculature of the CBA

539   mouse brain: A magnetic resonance imaging and micro computed tomography study.

540   *Neuroimage* 2007; 35: 1409–1423.

541 [18] Xiong B, Li A, Lou Y, et al. Precise Cerebral Vascular Atlas in Stereotaxic

542   Coordinates of Whole Mouse Brain. *Front Neuroanat* 2017; 11: 128.

543 [19] Deffieux T, Demene C, Pernot M, et al. Functional ultrasound neuroimaging: a

544   review of the preclinical and clinical state of the art. *Curr Opin Neurobiol* 2018; 50:

545   128–135.

546 [20] Hillman EMC. Optical brain imaging in vivo: techniques and applications from

547   animal to man. *J Biomed Opt*; 12: 051402.

548 [21] Hillman EMC. Coupling mechanism and significance of the BOLD signal: a status

549   report. *Annu Rev Neurosci* 2014; 37: 161–81.

550 [22] Kennerley AJ, Mayhew JE, Redgrave P, et al. Vascular Origins of BOLD and CBV

551   fMRI Signals: Statistical Mapping and Histological Sections Compared. *Open*

552   *Neuroimag J* 2010; 4: 1–8.

553 [23] Turner R. How much cortex can a vein drain? Downstream dilution of activation-

554   related cerebral blood oxygenation changes. *Neuroimage* 2002; 16: 1062–7.

555 [24] Grandjean J, Canella C, Anckaerts C, et al. Common functional networks in the

556   mouse brain revealed by multi-centre resting-state fMRI analysis. *Neuroimage* 2019;

557　　　　116278.

558　[25]　Tong Y, Hocke LM, Frederick BB. Low Frequency Systemic Hemodynamic 'Noise'

559　　　　in Resting State BOLD fMRI: Characteristics, Causes, Implications, Mitigation

560　　　　Strategies, and Applications. *Front Neurosci* 2019; 13: 787.

561　[26]　Dorr AE, Lerch JP, Spring S, et al. High resolution three-dimensional brain atlas

562　　　　using an average magnetic resonance image of 40 adult C57Bl/6J mice. *Neuroimage*

563　　　　2008; 42: 60–69.

564　[27]　Liska A, Galbusera A, Schwarz AJ, et al. Functional connectivity hubs of the mouse

565　　　　brain. *Neuroimage* 2015; 115: 281–291.

566　[28]　Jonckers E, Van Auderkerke J, De Visscher G, et al. Functional connectivity fMRI

567　　　　of the rodent brain: comparison of functional connectivity networks in rat and

568　　　　mouse. *PLoS One* 2011; 6: e18876.

569　[29]　Stafford JM, Jarrett BR, Miranda-Dominguez O, et al. Large-scale topology and the

570　　　　default mode network in the mouse connectome. *Proc Natl Acad Sci* 2014; 111:

571　　　　18745–18750.

572　[30]　Grandjean J, Canella C, Anckaerts C, et al. Common functional networks in the

573　　　　mouse brain revealed by multi-centre resting-state fMRI analysis. *Neuroimage* 2019;

574　　　　205: 116278.

575　[31]　Hess A, Hinz R, Keliris GA, et al. On the Usage of Brain Atlases in Neuroimaging

576　　　　Research. *Mol Imaging Biol*; 20. Epub ahead of print 2018. DOI: 10.1007/s11307-

577　　　　018-1259-y.

578   [32]   Ward R, Collins RL, Tanguay G, et al. A quantitative study of cerebrovascular

579   variation in inbred mice. *J Anat* 1990; 173: 87–95.

580   [33]   Barone FC, Knudsen DJ, Nelson AH, et al. Mouse Strain Differences in

581   Susceptibility to Cerebral Ischemia are Related to Cerebral Vascular Anatomy. *J*

582   *Cereb Blood Flow Metab* 1993; 13: 683–692.

583   [34]   Beckmann N. High resolution magnetic resonance angiography non-invasively

584   reveals mouse strain differences in the cerebrovascular anatomy in vivo. *Magn*

585   *Reson Med* 2000; 44: 252–8.

586   [35]   Barone FC, Knudsen DJ, Nelson AH, et al. Mouse strain differences in susceptibility

587   to cerebral ischemia are related to cerebral vascular anatomy. *J Cereb Blood Flow*

588   *Metab* 1993; 13: 683–92.

589   [36]   Hinz R, Peeters LM, Shah D, et al. Bottom-up sensory processing can induce

590   negative BOLD responses and reduce functional connectivity in nodes of the default

591   mode-like network in rats. *Neuroimage* 2019; 197: 167–176.

592

593

594   **Figure legends**

595   **Figure 1. Time of flight magnetic resonance imaging.** Example of a 2D-TOF MRA dataset of a

596   representative animal. Dataset included three orthogonally positioned 2D-TOF MRA scans with the

597   slice package placed (A) Coronally, (B) Axially and (C) Sagittally allowing the visualization of

598   vascular flow in the rostral-caudal, dorsal-ventral and left right direction respectively. Datasets were

599   combined using a maximum intensity projection (MIP) to visualize whole brain vasculature (D).

600   **Figure 2. Arterial System and vascular graph.** A. Three-dimensional overview of the arterial

601   system with annotations included in the vascular atlas. Crosshair indicates rostral-caudal (Ro-Ca),

602   dorsal-ventral (D-V) and left-right (L-R) direction. B. Hierarchical structure and annotations of the

603   mouse brain arterial system.

604   **Figure 3. Venous System and vascular graph.** A. Three-dimensional overview of the venous

605   system with annotations included in the vascular atlas. Crosshair indicates rostral-caudal (Ro-Ca),

606   dorsal-ventral (D-V) and left-right (L-R) direction. B. Hierarchical structure and annotations of the

607   mouse brain venous system.

608   **Figure 4. Skeletonization of the mouse brain vasculature.** A. The labeling of the vasculature was

609   skeletonized and is represented in nodes and edges. The nodes represent starting, end or bifurcation

610   points, while edges indicate vessel paths. Furthermore, the skeletonization process allows for fast

611   detection of arteries (red) and veins (blue) as both were detected as separate circuits B. When

612   comparing the labeled vasculature with the anatomical template, a discrepancy between vessel size

613   could be observed. Centerlines can be used to demonstrate the presence of a vessel irrespectively of

614   its size. For visualization purposes centerlines were depicted with a centerline thickness of 4 voxels.

615   **Figure 5. Resting state networks with highest vascular overlap.** Statistical map of two resting

616   state networks with highest vascular overlap (A) Cingulate-Retrosplenial I (0.21%) and (B)II

617   (0.17%). Statistical maps were produced by one sample t-test (p<0.001, uncorrected) performed on

618   the outcome of an independent component analysis. Color bar represents t-values.

619   **Figure 6. Resting state networks and vascular overlap.** 3D visual representation of the statistical

620   maps of (A) cingulate-retrosplenial I and (B) II network together with the brain vasculature (MIP).

621   Statistical maps were produced by one sample t-test (p<0.001, uncorrected) performed on the

622   outcome of an independent component analysis. Color bar represents t-values. Blood vessel that

623   partially overlap with the resting state network were highlighted in green.

624   **Table 1. Percent Vascular Inclusion (PVI) in Cingulate-Retrosplenial I and II.** Percentage

625   vessel of the vascular skeleton contained within the resting state component.

626

627   **Tables**

Vessel Name	Cingulate - Retrosplenial I (% vessel within component)	Cingulate - Retrosplenial II (% vessel within component)
Internal Carotid Artery (Right)	26.67	/
Internal Carotid Artery (Left)	28.57	/
Superior Cerebral Artery (Right)	15.38	5.13
Lateral Superior Cerebellar Artery (Right)	78.57	/
Lateral Superior Cerebellar Artery (Left)	52.38	/
Posterior Communicating Artery (Right)	8.33	/
Posterior Cerebral Artery (Right)	25.00	/
Posterior Cerebral Artery (Left)	21.57	/
Middle Cerebral Artery (Right)	11.59	10.14
Middle Cerebral Artery (Left)	5.63	5.63
Anterior Cerebral Artery (Right)	64.29	/
Anterior Cerebral Artery (Left)	31.03	/
Azygos of Anterior Cerebral Artery	27.27	/
Azygos Pericallosal Artery	41.82	50.91
Medial Orbitofrontal Artery	14.29	2.86
Superior Sagittal Sinus	13.58	24.53
Transverse Sinus (Right)	/	/
Transverse Sinus (Left)	22.73	/
Medial Collicular Vein (Left)	7.41	/
Straight Sinus	100.00	92.31
Inferior Sagittal Sinus	100.00	100.00
Vein of Galen	79.17	100.00
Longitudinal Hippocampal Vein (Right)	100.00	100.00
Longitudinal Hippocampal Vein (Left)	100.00	41.67
Thalamostriate Vein_(Right)	50,00	3.85
Thalamostriate vein (Left)	50.00	10.00

628   **Table 1. Percent Vascular Inclusion (PVI) in Cingulate-Retrosplenial I and II.**
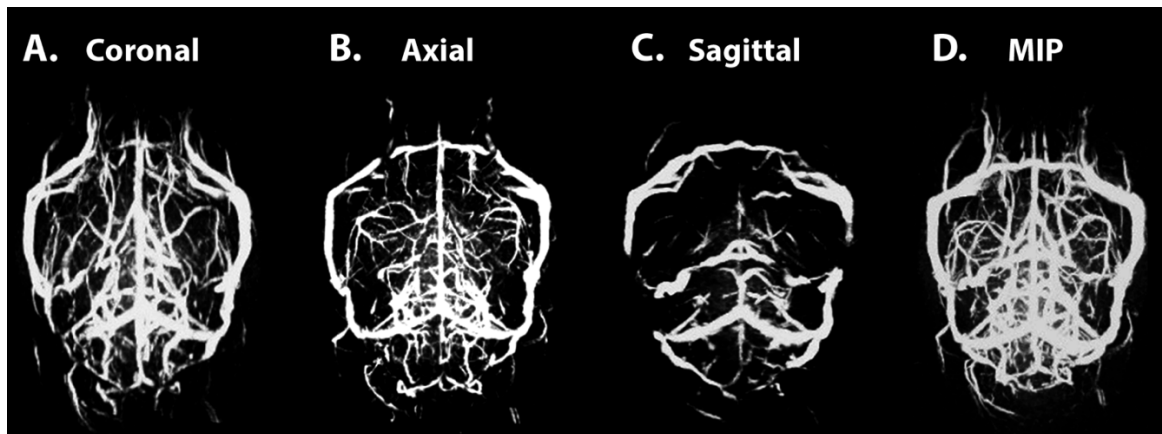
629 **Figures**

630

631 **Figure 1. Time of flight magnetic resonance imaging.** Example of a 2D-TOF MRA dataset of a
632 representative animal. Dataset included three orthogonally positioned 2D-TOF MRA scans with the
633 slice package placed (A) Coronally, (B) Axially and (C) Sagittally allowing the visualization of
634 vascular flow in the rostral-caudal, dorsal-ventral and left right direction respectively. Datasets were
635 combined using a maximum intensity projection (MIP) to visualize whole brain vasculature (D).

636
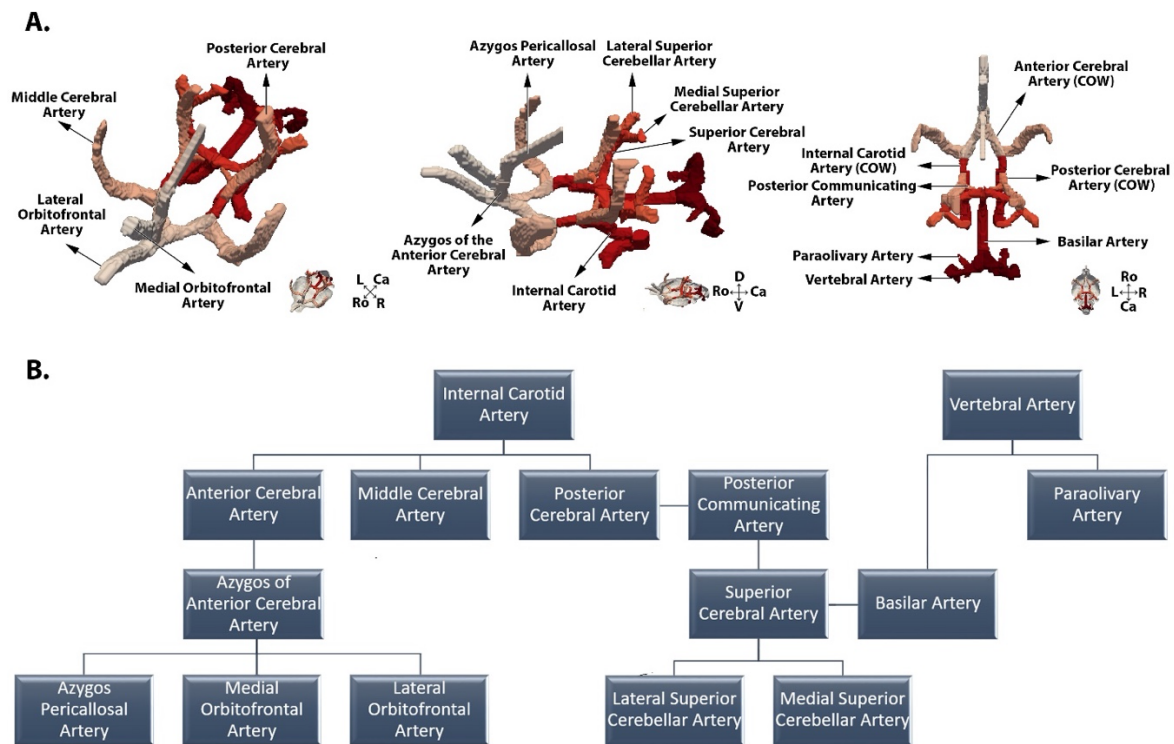
Figure 2. Arterial System and vascular graph. A. Three-dimensional overview of the arterial system with annotations included in the vascular atlas. Crosshair indicates rostral-caudal (Ro-Ca), dorsal-ventral (D-V) and left-right (L-R) direction. B. Hierarchical structure and annotations of the mouse brain arterial system.
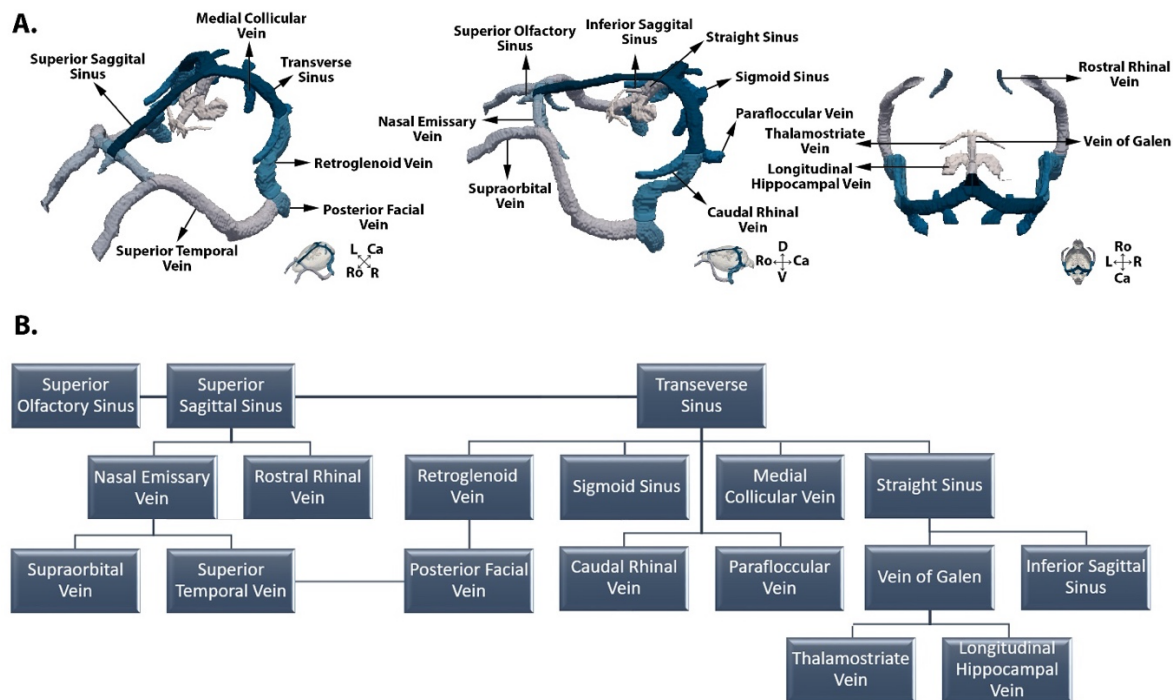
Figure 3. Venous System and vascular graph. A. Three-dimensional overview of the venous system with annotations included in the vascular atlas. Crosshair indicates rostral-caudal (Ro-Ca), dorsal-ventral (D-V) and left-right (L-R) direction. B. Hierarchical structure and annotations of the mouse brain venous system.
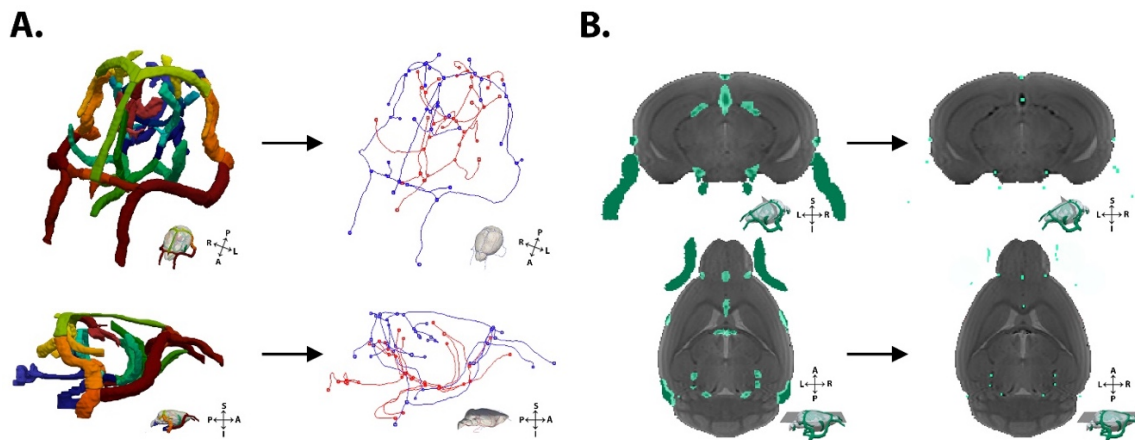
649

Figure 4. Skeletonization of the mouse brain vasculature. A. The labeling of the vasculature was skeletonized and is represented in nodes and edges. The nodes represent starting, end or bifurcation points, while edges indicate vessel paths. Furthermore, the skeletonization process allows for fast detection of arteries (red) and veins (blue) as both were detected as separate circuits B. When comparing the labeled vasculature with the anatomical template, a discrepancy between vessel size could be observed. Centerlines can be used to demonstrate the presence of a vessel irrespectively of its size. For visualization purposes centerlines were depicted with a centerline thickness of 4 voxels.
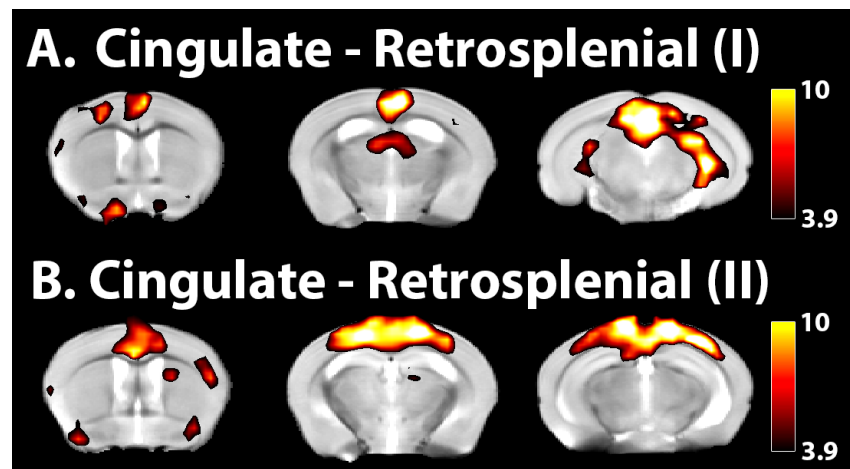
Figure 5. Resting state networks with highest vascular overlap. Statistical map of two resting state networks with highest vascular overlap (A) Cingulate-Retrosplenial I (0.21%) and (B)II (0.17%). Statistical maps were produced by one sample t-test (p<0.001, uncorrected) performed on the outcome of an independent component analysis. Color bar represents t-values.
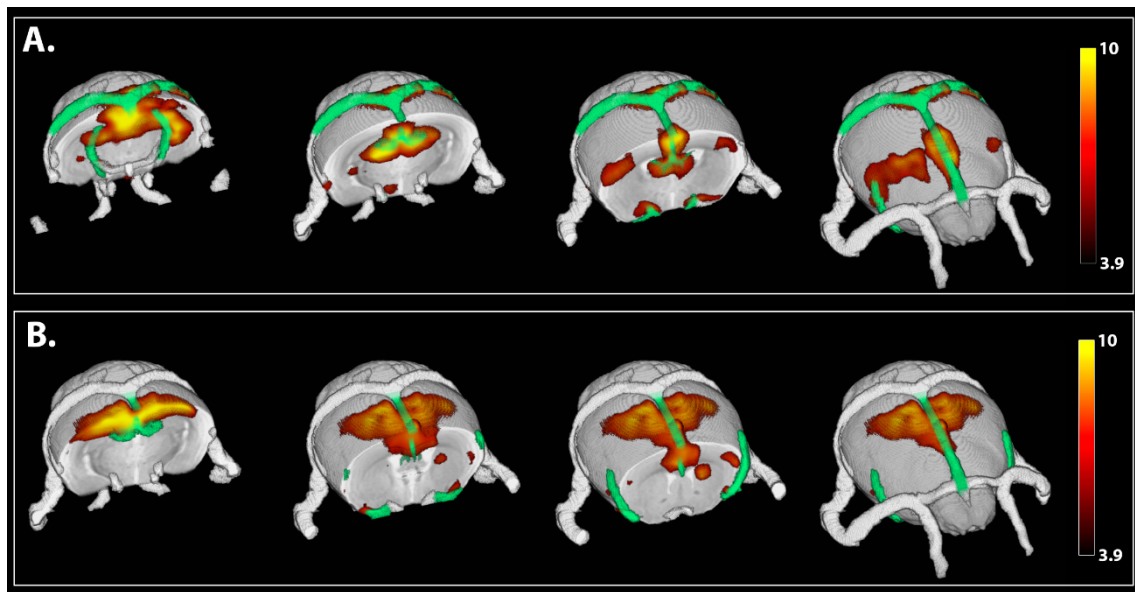
664

Figure 6. Resting state networks and vascular overlap. 3D visual representation of the statistical maps of (A) cingulate-retrosplenial I and (B) II network together with the brain vasculature (MIP). Statistical maps were produced by one sample t-test (p<0.001, uncorrected) performed on the outcome of an independent component analysis. Color bar represents t-values. Blood vessel that partially overlap with the resting state network were highlighted in green.